Radio Science

RESEARCH ARTICLE
10.1029/2019RS007004

Key Points:
- Severe scintillation is observed several consecutive days before 17 March 2015 in Hong Kong
- Significant scintillation events on signal-to-noise ratio and multipath observables are observed in the runup to the super magnetic storm
- The PPP performance is improved significantly with the combination of GPS/GLONASS/BDS during the ionospheric anomaly period

Correspondence to:
S. Ji,
jidifferent@gmail.com

Citation:
Lu, Y., Wang, Z., Ji, S., & Chen, W. (2020). Assessing the positioning performance under the effects of strong ionospheric anomalies with multi-GNSS in Hong Kong. *Radio Science*, *55*, e2019RS007004. https://doi.org/10.1029/2019RS007004

Received 2 OCT 2019
Accepted 11 JUL 2020
Accepted article online 15 JUL 2020

Author Contributions:
Conceptualization: Zhenjie Wang, Wu Chen
Formal analysis: Yangwei Lu
Methodology: Shengyue Ji
Supervision: Zhenjie Wang, Wu Chen
Writing - original draft: Yangwei Lu
Writing – review & editing: Shengyue Ji

Assessing the Positioning Performance Under the Effects of Strong Ionospheric Anomalies With Multi-GNSS in Hong Kong

Yangwei Lu[1,2], Zhenjie Wang[3,4], Shengyue Ji[3,4], and Wu Chen[2,5]

[1]National Time Service Center, Chinese Academy of Sciences, Xi'an, China, [2]Department of Land Surveying and Geo-informatics, Hong Kong Polytechnic University, Hong Kong, [3]Department of Surveying and Mapping, China University of Petroleum (East China), Qingdao, China, [4]Laboratory for Marine Mineral Resources, Qingdao National Laboratory for Marine Science and Technology, Qingdao, China, [5]Shenzhen Research Institute, Hong Kong Polytechnic University, Shenzhen, China

Abstract Global navigation satellite system (GNSS) precise positioning performance will be strongly affected under severe ionospheric anomaly conditions. The combination of multi-GNSS can increase the available observations and improve the geometry of continuously tracked satellites. This paper focuses on assessing the positioning performance with the combination of Global Positioning System (GPS), Global'naya Navigatsionnaya Sputnikova Sistema (GLONASS), and BeiDou System (BDS) around the St. Patrick's Day geomagnetic storm (9–18 March) in 2015 in Hong Kong. The rate of total electron content (TEC) index (ROTI) indicates severe ionospheric anomalies before the superstorm, while it was absent during the main phase of the storm in Hong Kong. Furthermore, strong scintillation events on signal-to-noise ratio (SNR) and multipath (MP) observables are observed during ionospheric anomalies period. Then the performance of single-point positioning (SPP) and precise point positioning (PPP) with multi-GNSS is shown. The ionospheric scintillation events may reduce pseudorange accuracy but affect SPP performance a little in this study, while the PPP accuracy is vastly decreased due to the subsequent reconvergence caused by frequent cycle slip (CS). Compared to PPP solutions with GPS only, the accuracy is improved significantly with the combination of multi-GNSS.

1. Introduction

Space weather affects the availability and accuracy of global navigation satellite system (GNSS) positioning, as it may lead to fluctuations of the radio navigation signals, cycle slip (CS), and loss of lock (LOL) (Ji, Chen, Wang, et al., 2013, Ji, Chen, Weng, et al., 2013, Prikryl et al., 2015; Liu et al., 2018; Yang & Liu, 2016). The effects of space weather on GNSS include the influence from ionospheric perturbations and the direct impact from solar radio bursts (Sreeja et al., 2014; Sreeja, 2016) and solar flares (Berdermann et al., 2018). Solar radio bursts are sudden intense radio emissions from the Sun in all wavelength and are often associated with solar flares. It can affect both the Earth's upper atmosphere and propagation of radio waves (Yasyukevich et al., 2018); it is more frequent and stronger near the solar maximum. The ionospheric perturbations result in amplitude and phase fluctuations in the received signal (Kintner et al., 2007; Xu et al., 2015; Vilà-Valls et al., 2017; Xu & Morton, 2018), a phenomenon known as scintillation. The major scintillation activity is usually observed during the solar maximum period, near the magnetic equator and in the midnight sector (Basu et al., 1988: Priyadarshi, 2015).

Several works have attempted to mitigate ionospheric scintillation effects on GNSS positioning accuracy, and these methods fall into three categories. The first is to adapt the stochastic model based on signal tracking variances (Aquino et al., 2009; Conker et al., 2003; da Silva et al., 2010). The second method employs the quality control algorithm to reject the contaminated observations by ionospheric anomalies (Zhang et al., 2014). The third method is to improve the positioning performance with multi-GNSS. There will be more and more available observations, and the positioning accuracy is expected to be improved with multi-GNSS. Marques et al. (2018) assessed the precise point positioning (PPP) accuracy under the ionospheric scintillation effects with multi-GNSS in Brazil. The positioning accuracy improvements was up to 60% under conditions of strong scintillation with the combination of GPS and GLONASS compared to GPS alone.

The St. Patrick's storm in 2015 is the first super geomagnetic storm during the 24 Solar Cycle 24 and has been gaining many researchers' attention. They mainly focus on two folds, that is, the ionospheric response and its effects on GNSS positioning service. They characterized the ionospheric irregularities of different regions, such as China (Ning & Tang, 2018; Sun et al., 2017), Norway (Jacobsen & Andalsvik, 2016), India (Yadav et al., 2016), high-latitude region (Cherniak et al., 2015), low-latitude region (Maurya et al., 2018), South America (Barbosa et al., 2018), African equatorial/low-latitude region (Amaechi et al., 2018), European-African region (Borries et al., 2016), and the global scale. At the same time, they also used different instruments or data, including ground-based GNSS data, ionosondes data, TSX data, GRACE data, Swarm data, GUVI, Jason-2, and GPS data on Jason-2 for understanding the geomagnetic storm (Astafyeva et al., 2015; Chen et al., 2016; Jin et al., 2017; Kuai et al., 2016; Nava et al., 2016; Prikryl et al., 2016). Meanwhile, the GPS scintillation events, LOL, and its effects on positioning service during the main phase were also demonstrated (Jacobsen & Andalsvik, 2016; Jin & Oksavik, 2018; Luo et al., 2018).

As described by Helmboldt et al. (2015), there were many solar flares of varying magnitudes in the runup to the G4-class geomagnetic storm of St. Patrick's Day in 2015. Furthermore, Hong Kong is located in the low-latitude region; the ionospheric anomaly events peak around March and September (Gao, 2008; Hlubek et al., 2014; Ji, Chen, Wang, et al., 2013). GNSS receivers in Hong Kong are expected to observe more anomaly around this period.

This contribution focuses on improving the positioning performance with the combination of GPS, GLONASS, and BDS around the St. Patrick's storm in 2015 in Hong Kong. After a brief introduction of multi-GNSS data processing algorithm, we first demonstrate the space weather and ionosphere conditions around St. Patrick's Day in 2015 by an overview. Then the ionospheric anomaly effects on GNSS measurements including signal-to-noise ratio (SNR) and multipath (MP) observable are shown. Finally, The single-point positioning (SPP) and PPP performance with multi-GNSS and GPS alone are systematically assessed.

2. Data Sets and Methodology

2.1. The Rate of Total Electron Content Index

For most of the users, the S4 index is not available; the rate of total electron content (TEC) index (ROTI) is employed to measure the ionospheric scintillation indirectly. The ROTI reflects the fluctuations in ionospheric TEC, which denotes ionospheric anomaly presence. It is defined as the standard deviation of the rate of TEC (ROT) over some time interval (Jacobsen, 2014; Pi et al., 1997); usually, 5 min is adopted.

$$\mathrm{ROTI}(i) = \sqrt{\frac{1}{N}\sum_{j=i-N}^{i}\left(\mathrm{ROT}(j) - \overline{\mathrm{ROT}}\right)^2} \tag{1}$$

where N is the total number of ROT epoch, $\overline{\mathrm{ROT}}$ is the mean value of ROT over N epoch, and ROT is the rate of TEC change at j time-epoch. It can be calculated as follows:

$$\mathrm{ROT}(j) = \frac{\mathrm{TEC}(j) - \mathrm{TEC}(j-1)}{t_j - t_{j-1}} \tag{2}$$

where $t_j - t_{j-1}$ is the time difference between the epoch j and $j-1$.

The geometry-free (GF) phase combination is introduced to compute slant TEC (STEC); it can be read as

$$L_{\mathrm{GF}} = L^s_{1,r} - L^s_{2,r} = -\left(\frac{1}{f_1^2} - \frac{1}{f_2^2}\right)40.3{*}10^{16}{*}\mathrm{STEC} + B \tag{3}$$

where L_{GF} is the GF phase combination observation; r and s refer to receiver and satellite; $L^s_{1,r}$ and $L^s_{2,r}$ are the carrier phase measurements in meters at frequencyL_1, L_2; f is the frequency of the carrier; $B{=}-\lambda_1\left(b^s_{1,r} + N^s_{1,r}\right) + \lambda_2\left(b^s_{2,r} + N^s_{2,r}\right)$ is a constant bias due to the phase ambiguities ($N^s_{1,r}$ and $N^s_{2,j}$) and instrument delay from receiver and satellite($b^s_{1,r}$ and $b^s_{2,j}$); and λ is the wavelength of carrier phase.

2.2. Code MP Observable

The MP observable is employed to analyze the characteristics of MP effects, which can be expressed as follows (Wang et al., 2015):

$$MP_j = P_j - \frac{f_j^2 + f_i^2}{f_j^2 - f_i^2} L_j + \frac{2f_i^2}{f_j^2 - f_i^2} L_i - B \tag{4}$$

where subscripts i, j are the carrier frequencies; P is the observed pseudorange; f denotes the carrier-phase frequency in Hertz; and B is the sum of phase ambiguity and constant part of hardware delay.

The MP combination is both ionosphere-free (IF) and GF. After removing the constant term, the residual mainly contains code MP and noise. Because the MP observable involves both pseudorange and carrier phase measurements, it is sensitive to CS and LOL.

2.3. GNSS Positioning Models

In this paper, the SPP solution is obtained by utilizing single-frequency observation; the ionospheric and tropospheric delay are corrected with Klobuchar (1987) model and Saastamoinen (1972) model, and the details can be referred to Takasu and Yasuda (2009).

The PPP solution in this paper is obtained with dual-frequency IF combination observations. The GNSS code and carrier phase IF combination can be defined as (Shi & Gao, 2014)

$$\begin{cases} P_{IF,r}^{\mathrm{m,s}} = \dfrac{1}{f_{m,1}^2 - f_{m,2}^2}\left(f_{\mathrm{m},1}^2 P_{1,r}^{m,s} - f_{\mathrm{m},2}^2 P_{2,r}^{m,s}\right) \\ L_{IF,r}^{\mathrm{m,s}} = \dfrac{1}{f_{m,1}^2 - f_{m,2}^2}\left(f_{\mathrm{m},1}^2 L_{1,r}^{m,s} - f_{\mathrm{m},2}^2 L_{2,r}^{m,s}\right) \end{cases}. \tag{5}$$

where m, r, and s refer to the satellite system, receiver, and satellite; and $P_{IF,r}^{\mathrm{m,s}}$ and $L_{IF,r}^{\mathrm{m,s}}$ are the pseudorange and carrier phase IF combination observations.

The IF PPP function model for GPS, GLONASS and BDS can be written as follows (Shi et al., 2017):

$$\begin{cases} P_{IF,r}^{G,s} = \rho_r^{G,s} + d_{orb}^{G} - c*dt^{G,s} + c*dt_r^{G} + m_r^{G,s}*T + \varepsilon\left(P_{IF,r}^{G,s}\right) \\ L_{IF,r}^{G,s} = \rho_r^{G,s} + d_{orb}^{G} - c*dt^{G,s} + c*dt_r^{G} + m_r^{G,s}*T + B_{IF,r}^{G,s} + \varepsilon\left(L_{IF,r}^{G,s}\right) \end{cases} \tag{6}$$

$$\begin{cases} P_{IF,r}^{R,s} = \rho_r^{R,s} + d_{orb}^{R} - c*dt^{R,s} + c*dt_r^{G} + c*dt_{sys}^{R} + m_r^{R,s}*T + \varepsilon\left(P_{IF,r}^{R,s}\right) \\ L_{IF,r}^{R,s} = \rho_r^{R,s} + d_{orb}^{R} - c*dt^{R,s} + c*dt_r^{G} + c*dt_{sys}^{R} + m_r^{R,s}*T + B_{IF,r}^{R,s} + \varepsilon\left(L_{IF,r}^{R,s}\right) \end{cases} \tag{7}$$

$$\begin{cases} P_{IF,r}^{C,s} = \rho_r^{C,s} + d_{orb}^{C} - c*dt^{C,s} + c*dt_r^{G} + c*dt_{sys}^{C} + m_r^{C,s}*T + \varepsilon\left(P_{IF,r}^{C,s}\right) \\ L_{IF,r}^{C,s} = \rho_r^{C,s} + d_{orb}^{C} - c*dt^{C,s} + c*dt_r^{G} + c*dt_{sys}^{C} + m_r^{C,s}*T + B_{IF,r}^{C,s} + \varepsilon\left(L_{IF,r}^{C,s}\right) \end{cases} \tag{8}$$

where G, R, and C indicate the GNSS index (G:GPS, R:GLONASS, and C:BDS); dt_r^G is the receiver clock of GPS; and dt_{sys}^R and dt_{sys}^C are the system time difference parameters for GLONASS and BDS with respect to GPS, respectively. P, L, and ρ are the pseudorange, carrier phase, and geometry distance between receiver and satellite, respectively. T is the zenith tropospheric delay; m is troposphere mapping function; B is the corresponding IF float ambiguity; ε is the measurement noise; and c is the speed of light in vacuum. d_{orb}^G is the satellite orbit error; $dt^{G,s}$ is satellite clock error.

Then the Bernese5.2 (Dach et al., 2015) and GAMP (Zhou et al., 2018) software are employed to estimate the related parameters including coordinates, receiver clock bias, the system bias of GLONASS/BDS relative to GPS, zenith tropospheric wet delay, and ambiguities.

2.4. Data Sets

The GNSS data used in this study were collected from six stations with Trimble NetR9 receiver (from 9 to 18 March 2015, ftp://ftp.geodetic.gov.hk/rinex3/2015/) in Hong Kong (Figure 1). The Kp, Dst, AE indexes, and X-ray fluxes were also downloaded to analyze the space weather conditions.

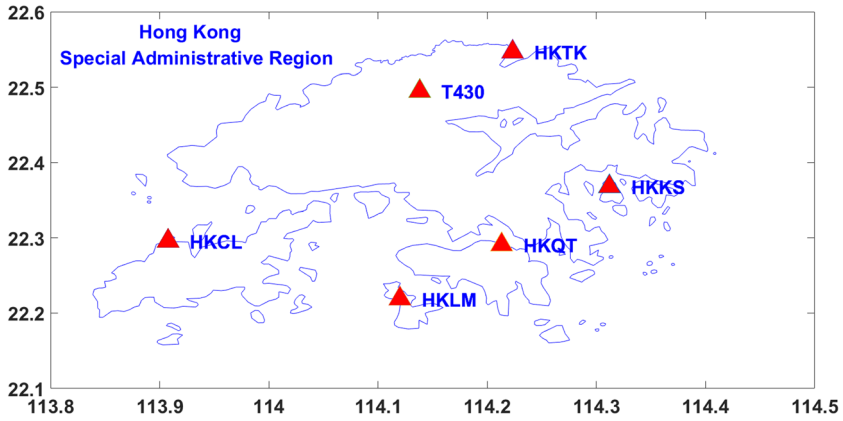

Figure 1. GPS stations in Hong Kong.

The Kp, Dst, AE, and its constituents AU and AL were obtained from World Data Center (WDC, http://wdc.kugi.kyoto-u.ac.jp). The solar flare X-ray measurements were obtained from the National Oceanic and Atmospheric Administration (NOAA, https://www.ngdc.noaa.gov/stp/spaceweather.html) in 1–8 Å and 0.5–4 Å wavelength ranges with a time resolution of 3 s. The X-ray fluxes are measured by the X-ray sensors on Geosynchronous Operational Environmental Satellite-15 (GOES-15) (Mahajan et al., 2010).

3. Space Weather and Ionospheric Conditions Around the St. Patrick's Storm in 2015

3.1. Space Weather Conditions

The Kp, Dst, AE, AU, and AL during 09–18 March 2015 are shown in Figure 2. According to the classification from Loewe and Prölss (1997), the thresholds of different indexes are shown with dotted lines. For the Kp and Dst indexes, the four dotted lines are the weak, moderate, strong, and severe storm class; both of them do not reach the great-class storm, while the AE, AU, and AL indexes indicate that it reached the great-class level several times during the main phase of the St. Patrick's storm.

As reported, the space weather is very complicated during March 2015; many M-class solar flares occurred in the runup to the St. Patrick's super magnetic storm (Helmboldt et al., 2015). Figure 3 shows the X-ray

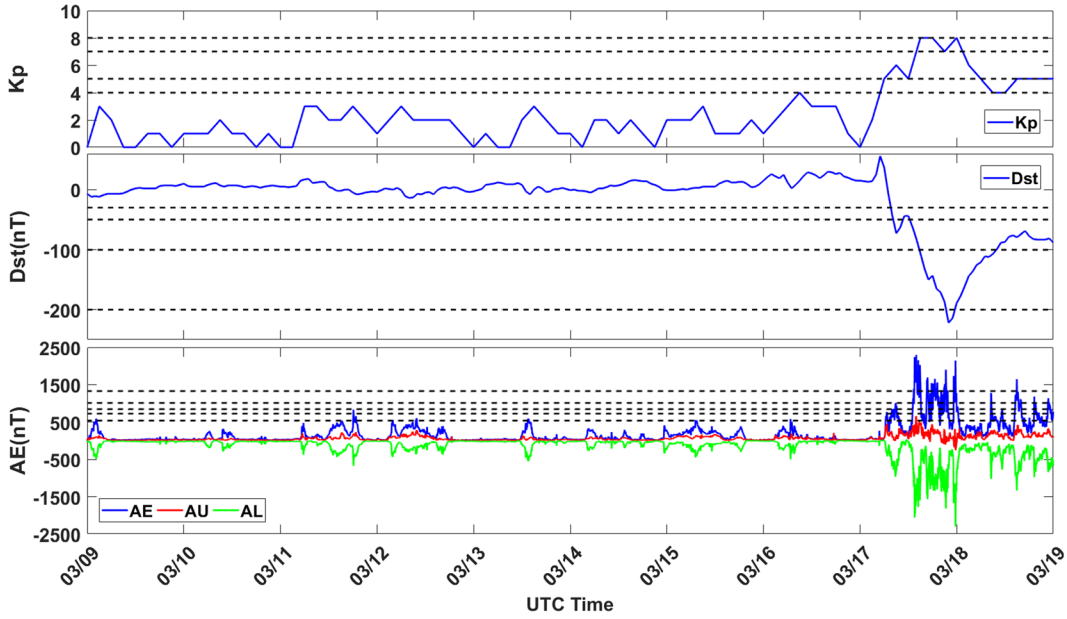

Figure 2. Geomagnetic conditions in March 2015.

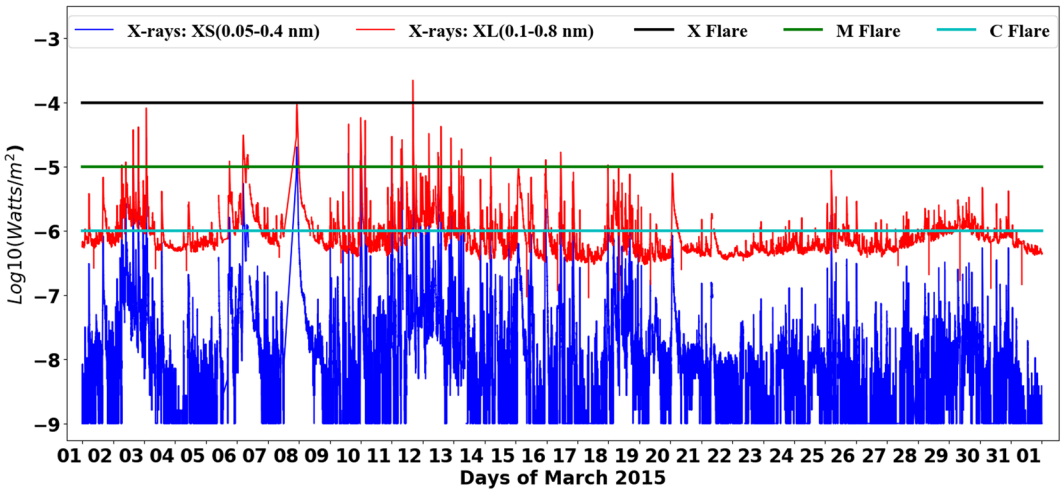

Figure 3. Geomagnetic conditions in March 2015.

irradiance measured by the GOES15 satellite, which indicates the occurrence of solar flares. The GOES data show that one X-class flare on 11 March was exactly X2.2; there were several M-class flares between 2 and 18 March and many C-class flares. After 18 March, there are only some C-class solar flares.

On the whole, the space weather before the St. Patrick's magnetic storm is much more disturbed than that after the St. Patrick's storm and reached the most disturbed condition on St. Patrick's Day. Especially for the period between 9 and 18 March, there is at least one M-class flare in each day, while the Kp, Dst, and AE indexes show absence of anomalies before 17 March and reached the peak value on 17 March.

3.2. Ionospheric Conditions

Figure 4 demonstrated the ROTI at Stations HKCL and HKKS. The plots indicate high consistency for ROTI between the two stations. In addition, the significant fluctuations of ROTI can be observed for both stations, especially on 9 and 11–16 March from 12:00 to 16:00 (local time: 20:00–24:00). During the main phase of the St. Patrick's magnetic storm (17 and 18 March), there are also jumps for ROTI, but the amplitude is much smaller than that of the days before in this study. As we know, ROTI indicates small scale irregularities of the ionosphere. This means there is no significant ionospheric anomaly observed during the main phase

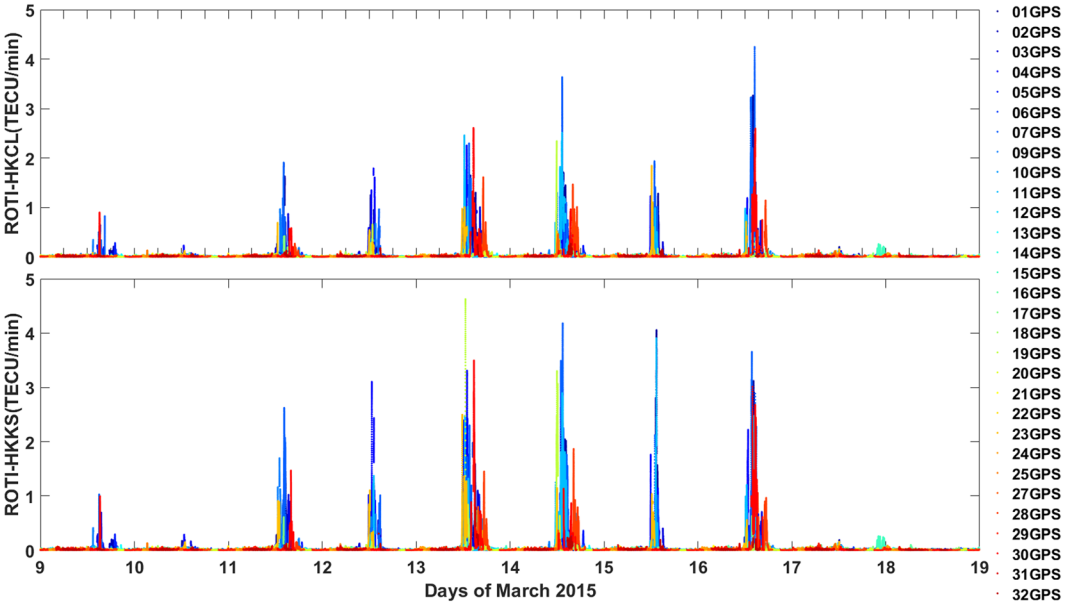

Figure 4. GPS ROTI variations measured at HKCL and HKKS.

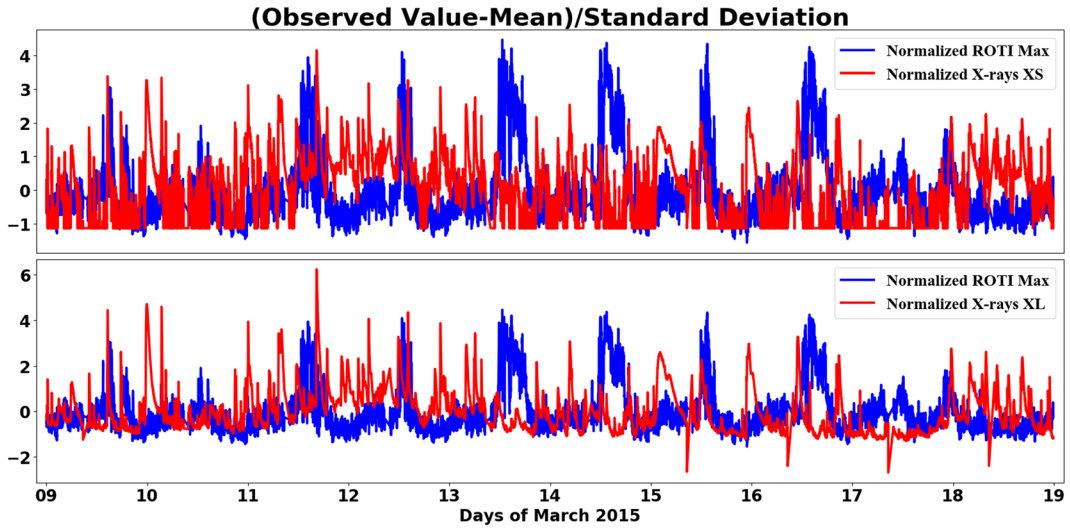

Figure 5. Normalized ROTI of HKKS and X-rays flux.

of the St. Patrick's magnetic storm in Hong Kong, while severe ionospheric anomalies are detected several consecutive days before the storm. It is similar to the ionospheric response of African equatorial/low-latitude (Amaechi et al., 2018) and the Taiwanese longitudinal sectors (Nayak et al., 2017). Thus, the observed ionospheric anomaly may be associated with ionospheric scintillation events.

According to the analysis in section 3.1, all the geomagnetic indexes including Kp, Dst, and AE indicate the quiet conditions of space weather from 9 to 16 March, except the X-ray. That is to say, there was absence of geomagnetic anomaly in Hong Kong, while the anomalies were observed through ROTI and X-ray flux during those days. Comparing Figures 3 and 4, we can conclude that when the X-ray fluxes reached the peak value (single X or M flare, or many C flares), there might be also a peak value for ROTI within 1 day for both GPS stations, especially for X-ray at 0.1–0.8 nm. In addition, the normalized ROTI of HKKS and X-ray flux are shown in Figure 5. The correlation can be observed to some extent, though the occurrence time of peak value for ROTI and X-ray flux are not exactly the same. As shown in Figure 5, there might be ROTI anomaly after 1.0–1.5 days when X-ray flux anomaly occurred. As we know, the ionosphere is built by absorbing soft X-rays and solar extreme ultraviolet (EUV) mainly at wavelengths below 105 nm (Vaishnav et al., 2018).

Furthermore, a daily increased ionospheric anomaly occurrence is expected in the equatorial region during the start of the equinox period (Steenburgh et al., 2008). In order to confirm that the TEC fluctuations are associated with solar X-ray flares, we examined the counts of EUV in March 2015. The anomalies of EUV counts are observed every day in March 2015 for all the five channels (Figure 6).

The X-ray and ROTI measurements strongly indicate disturbed space weather during 9–16 March except 10 March, while the Kp, Dst, and AE are less efficient to observe the effect of geomagnetic storm. As a consequence, position solutions are expected to be worst during that period and shown in the following section.

4. Positioning Performance With Multi-GNSS

In this section, the effects of ionospheric anomalies on GNSS are analyzed, including the fluctuations of SNR, MP observables, and performance of SPP and PPP with multi-GNSS.

4.1. Effects of Ionospheric Anomalies on SNR and MP Observables

The signal intensity attenuation led by ionospheric anomaly can be observed with the SNR measurements (Bong et al., 2015; He et al., 2016; Vadakke Veettil et al., 2017). Even more, the attenuation will affect the accuracy of pseudorange to some degree. The serious signal attenuation may result in CS or LOL for carrier phase measurements, which will affect the performance of GNSS precise positioning including PPP and real-time kinematic (RTK) positioning. The SNR observable used in this paper is indeed the C/N_0 obtained from RINEX file.

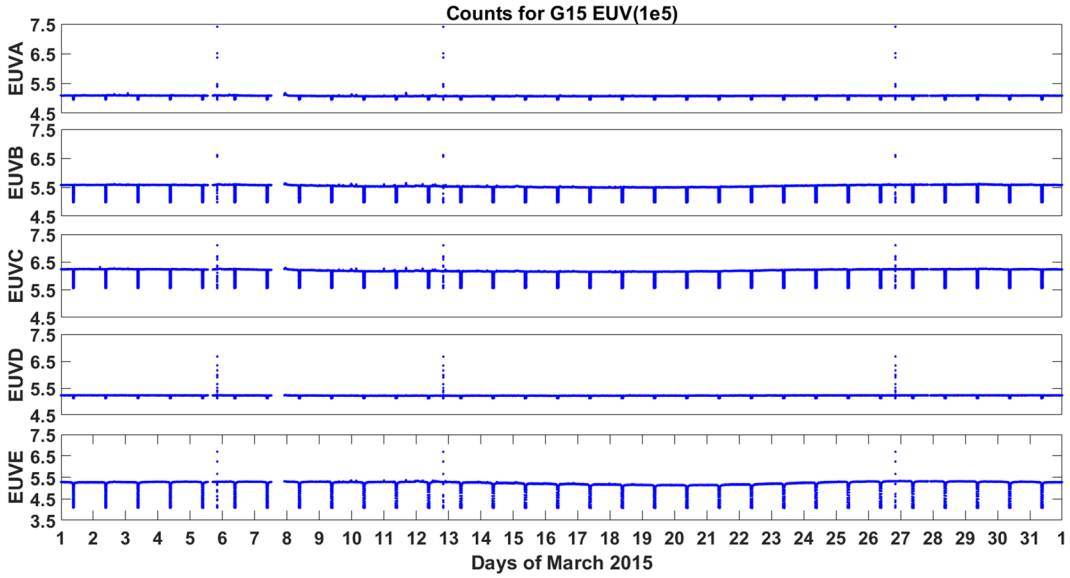

Figure 6. Counts for G15 EUV of March 2015.

The plots in Figure 7 demonstrate the SNR and MP observables of BDS C01 and C02 at HKCL from 9 to 18 March 2015. The significant scintillation events in both SNR and MP observables are observed except on 10, 17, and 18 March. The observed scintillation events can be grouped into two types: moderate and intense scintillation according to the fluctuation of SNR observable. The scintillation events with SNR fluctuation within 10 dB-Hz are grouped into moderate scintillation; the scintillation with SNR fluctuation more than 10 dB-Hz are grouped into intense scintillation. As shown in Figure 7, the examples with dotted box is moderate scintillation, the SNR is continuous, and its fluctuation is not more than 10 dB-Hz. The SNR series with solid-line box is regarded as intense scintillation in this paper. The examples of SNR in Figure 7 demonstrate

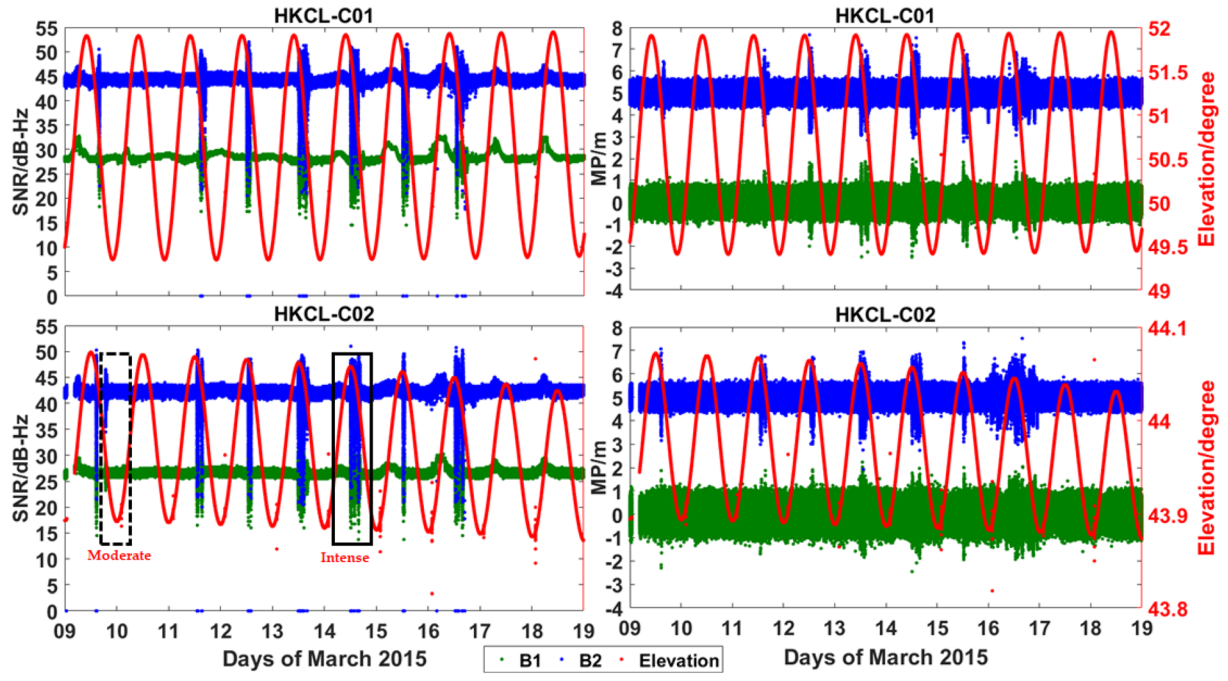

Figure 7. C01 and C02 SNR and MP observables of BDS at HKCL from 9 to 18 March 2015 (the SNR of B1 was shifted by −10, and the MP observable of B2 was shifted by 5).

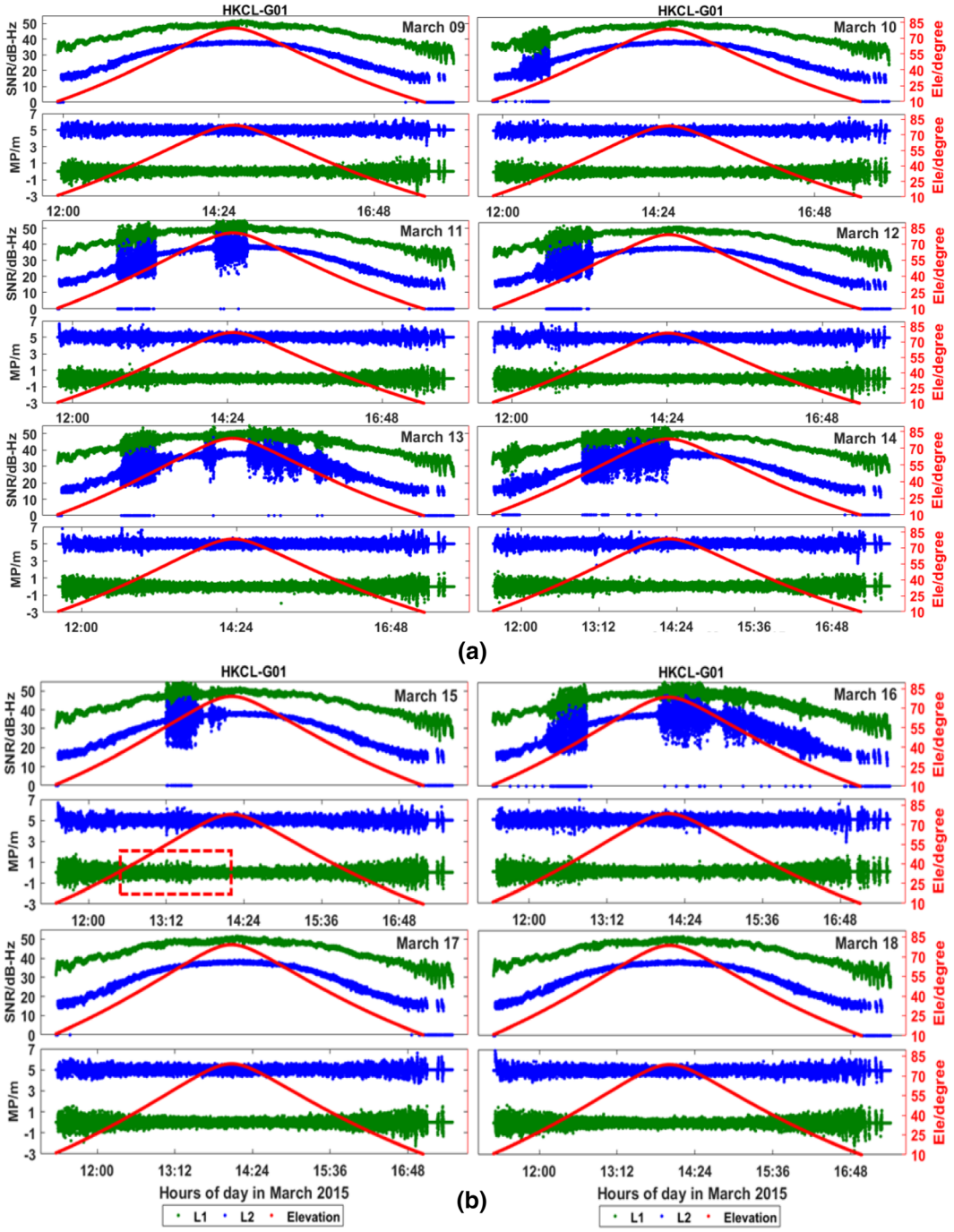

Figure 8. G01 SNR and MP observables at HKCL (the MP of L2 was shifted by 5).

that the intense scintillation is observed every day except on 10, 17, and 18 March from 9 to 18 March 2015, both for C01 and C02. The occurrence time of SNR fluctuations is consistent with the occurrence time of ROTI anomalies. The fluctuations of MP are consistent with that of SNR for most intense scintillation cases both for C01 and C02 except the B1 MP of C01 on 9 March. Furthermore, we found the SNR fluctuations for B2 frequency is much greater than that of B1 frequency (Figure 7). For example, the SNR fluctuations are about 10 dB-Hz for B1, while the maximum fluctuation more than 20 dB-Hz for B2. The MP observables of B2 also fluctuated more than MP of B1. That is the scintillation in B2 is more intense than that of B1 for BDS.

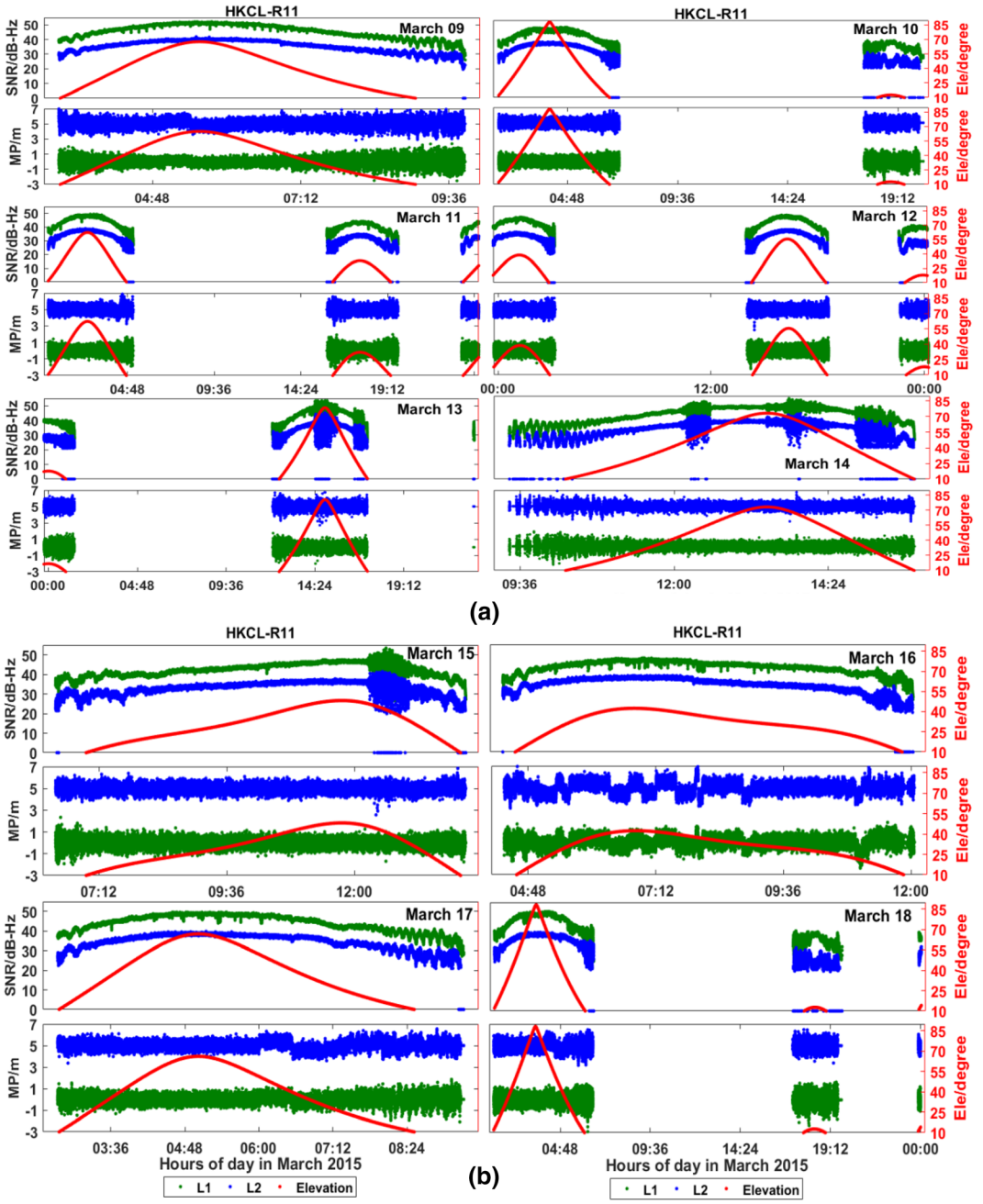

Figure 9. R11 SNR and MP observables at HKCL (the MP of L2 was shifted by 5).

Furthermore, the strange phenomenon observed from Figure 7 is that intermittent scintillation is observed during the whole day on 16 March from SNR and MP series both for C01 and C02. And the scintillation in MP series is much more significant than that of SNR, which may be led by CS and LOL caused by other factors. Figure 8 demonstrates the SNR and MP observables of GPS G01 both for L1 and L2. Significant fluctuations are observed in SNR from 10 to 16 March, while there is absence of scintillation on 17 and 18 March, the main phase of this storm. The MP is also affected at the same time as SNR, but amplitude is not significantly visible in Figure 8. The plots in Figure 9 are the SNR and MP series of GLONASS R11 for the 10 days. Because satellite orbit repeating period of GLONASS is 8 days (Ray et al., 2013), it cannot observe the scintillation every day for one satellite. During the 10 days, we observed scintillation on 13–15 March. On 16 March, the SNR series show many intermittent fluctuations, and the MP observables also fluctuate during

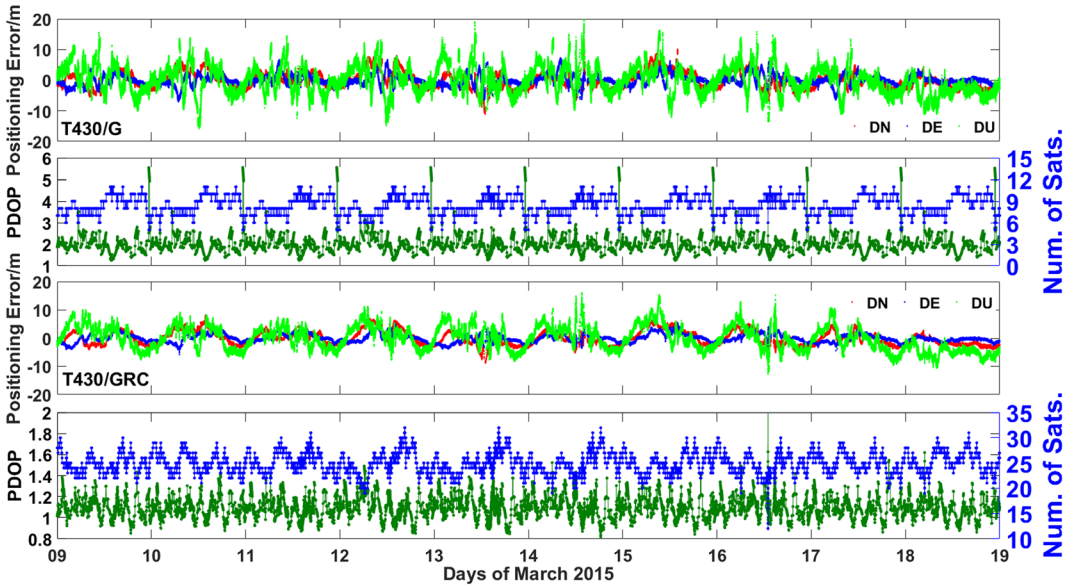

Figure 10. SPP results with single-frequency observations at T430 (G is GPS; GRC is the combination of GPS/GLONASS/BDS).

the corresponding period. While the GLONASS SNR fluctuation pattern on 16 March (Figure 9) is not similar to that of scintillation examples and the magnitude of fluctuation is also very small, we think this fluctuation may be related to MP.

The plots in Figures 7–9 indicate the occurrence time of SNR and MP fluctuations for GPS/GLONASS/BDS is consistent with the ROTI anomaly period, which mainly occurred between 12:00 and 16:00 (local time: 20:00–24:00) from 9 to 16 March except 10 March. Similar fluctuations are absent during the main phase of the geomagnetic storm on 17 and 18 March. The MP fluctuations vary with satellite system. The occurrence of MP fluctuations for BDS is much more frequent than that of GPS/GLONASS for this case, the SNR fluctuations do not lead to MP fluctuation for GPS/GLONASS sometimes. The duration and magnitude of MP fluctuations for BDS is also longer and bigger than those of GPS/GLONASS. Meanwhile, the Figures 7–9 also show that the scintillation events did not occur for all the satellites at the same time, as the satellites are distributed in different positions and satellite orbit repeated period varies a lot with satellite system and type. The MP observable is the GF and IF combination; its fluctuation indicates the pseudorange error, CS, and LOL. The rapid long-period fluctuations mainly result from CS or LOL; the others are led by pseudorange error. For example, the MP fluctuations in Figure 7 are caused by frequent CS and LOL, while the MP fluctuations in Figure 8b with red dotted box are contributed by pseudorange error led by rapid SNR fluctuations. We also examined the SNR and MP series of other stations in Hong Kong. The scintillation can be observed from all six stations every day from 9 to 16 March except 10, 17, and 18 March.

4.2. SPP Performance With Multi-GNSS

The SPP results are calculated with the RTKLIB software (Takasu & Yasuda, 2009) both for GPS-only and the combination of GPS/GLONASS/BDS. Figure 10 demonstrates the SPP positioning error (single-frequency observation), visible satellite number, and position dilution of precision (PDOP) value with elevation angle above 10°for GPS-only and GPS/GLONASS/BDS at T430. During the 10 days, the positioning accuracy with GPS only is very low (except 18 March), especially during the nighttime (local time). Furthermore, the positioning accuracy is improved with the combination of GPS/GLONASS/BDS.

Hong Kong is located in the ionospheric crest area from 9 to 17 March, which may lead to large difference between Klobuchar model and real ionospheric conditions. Then the SPP accuracy with single-frequency observation is very low for large uncorrected ionospheric error. Of course, the scintillation may also contribute to the accuracy decrease, but we think it is not the main reason for no significant jump observed during scintillation time.

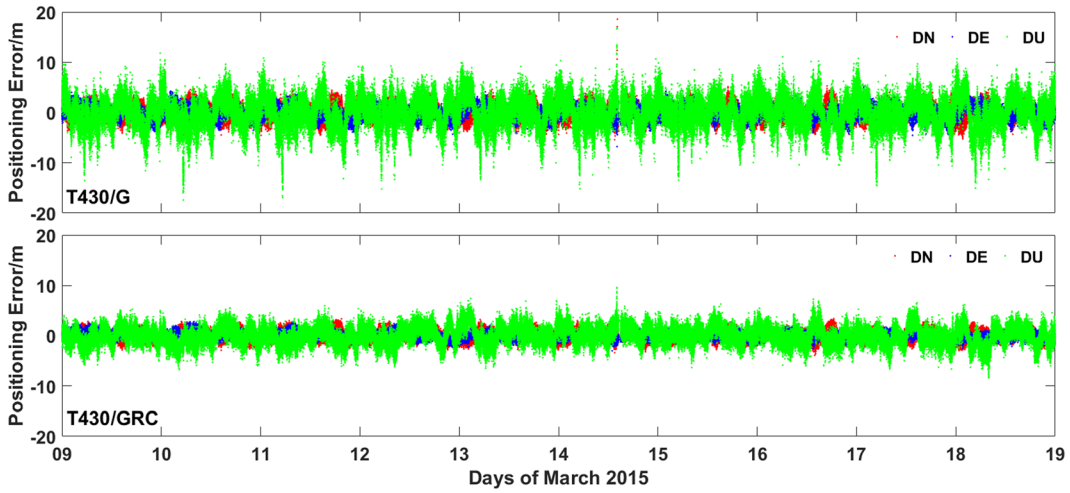

Figure 11. SPP results with code IF observations at T430 (G is GPS; GRC is the combination of GPS/GLONASS/BDS).

In order to confirm the above analysis, the code IF observation was employed to calculate receiver position. As the code IF combination eliminates the first-order ionospheric delay, the positioning accuracy is expected to be improved even with GPS only. Figure 11 shows the positioning error with code IF observation for GPS only and GPS/GLONASS/BDS at T430. The positioning accuracy with code IF observation is improved significantly compared to the results with single-frequency observations for GPS only, especially for the period of 9–17 March. When the code IF observations of GPS/GLONASS/BDS are employed, the accuracy is improved further as expected. This confirms the large difference between Klobuchar model and real ionospheric conditions, which reduce the accuracy for single-frequency SPP from 9 to 17 March. However, even

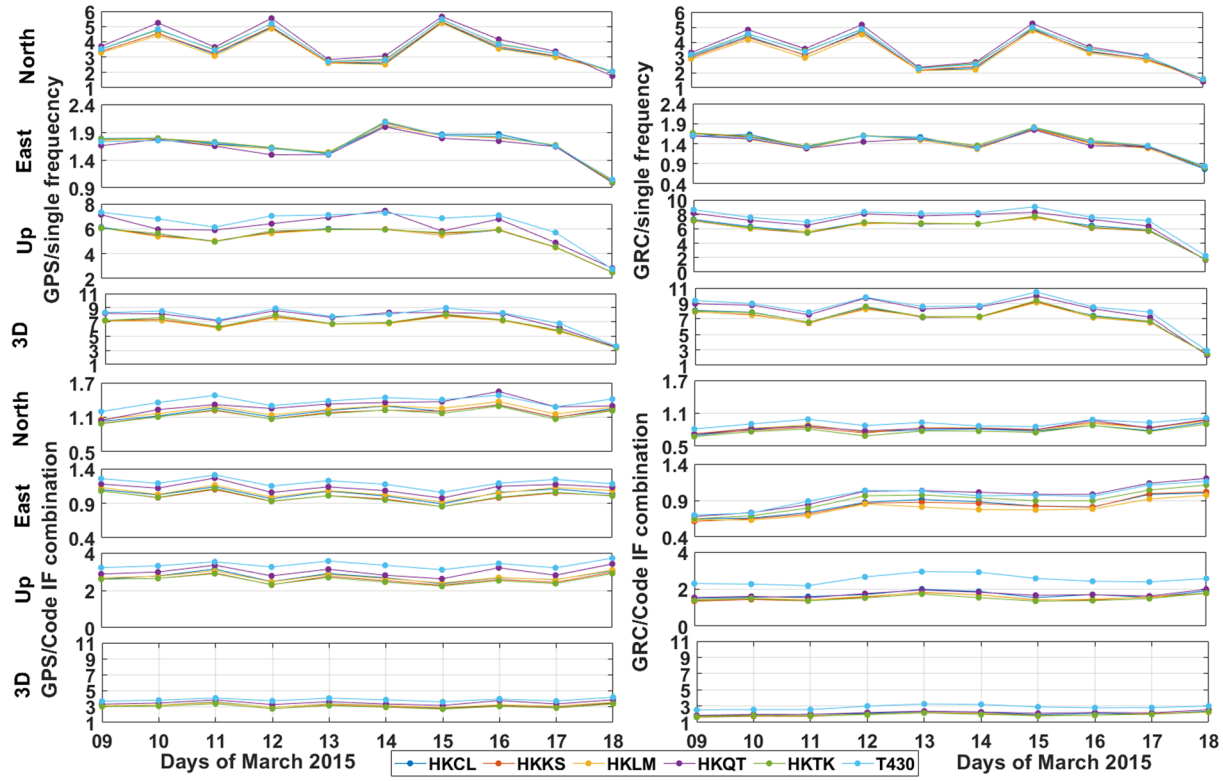

Figure 12. RMS (unit: m) of SPP for GPS only and combination of GPS/GLONASS/BDS (GRC) with single-frequency and code IF observations.

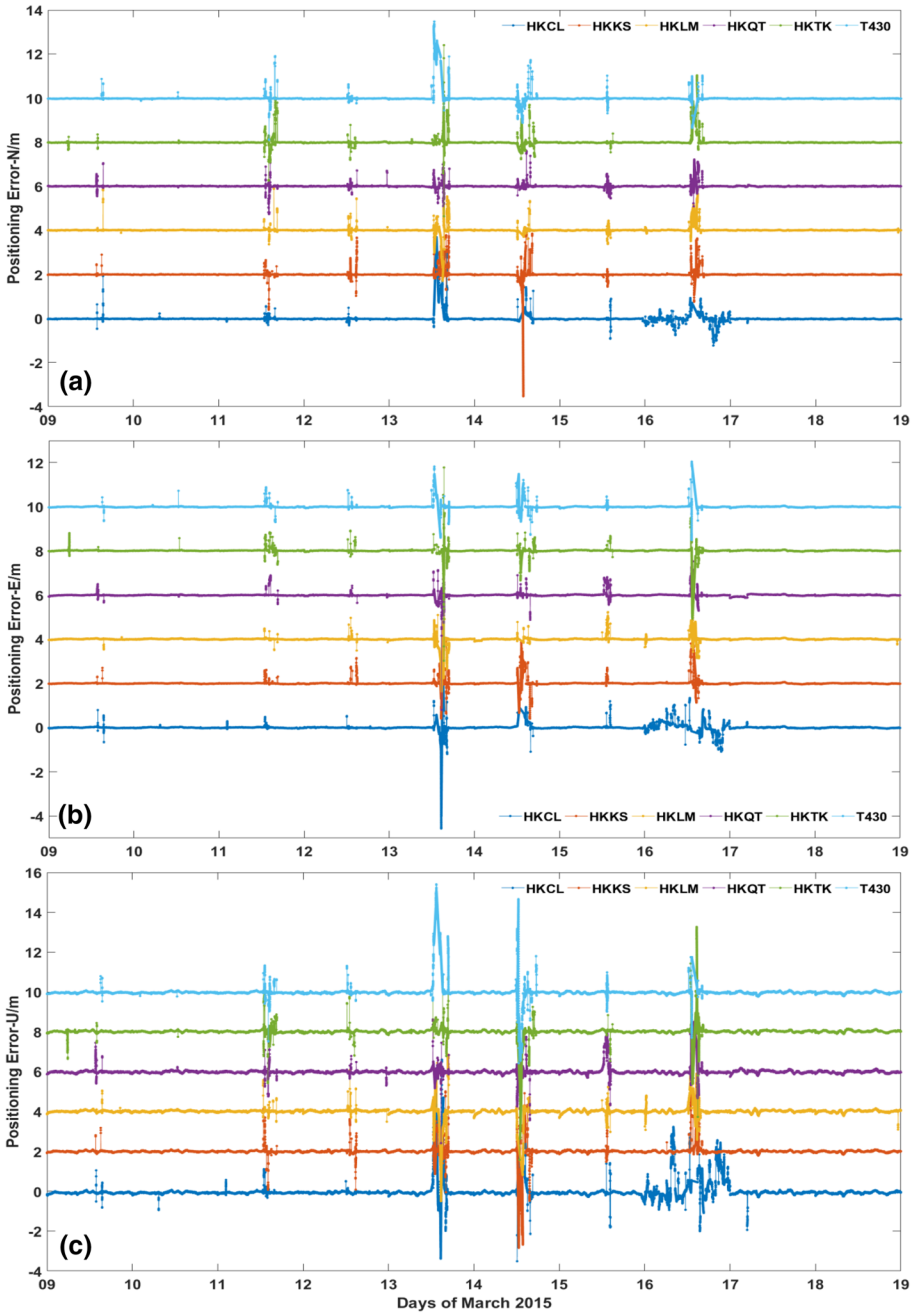

Figure 13. PPP results with GPS only at six stations in Hong Kong. The positioning error of each station was shifted by two additional meters except HKCL.

when the code IF observation is adopted, it is difficult to observe the direct relation between the SPP positioning error and SNR anomalies.

The root-mean-square (RMS) of SPP is shown in Figure 12. The statistical results confirm that the positioning error is not related to ionospheric anomalies both for single-frequency and code IF combination results. For single-frequency results, the positioning error does not show any clear correlation with ionospheric anomaly. Meanwhile, the positioning accuracy during 9 to 17 March is much lower than that of 18 March. After checking the global TEC map, the depletion of TEC is observed on 18 March.

Comparing to the results with single-frequency observations, the positioning accuracy is improved significantly with code IF observations both for GPS and GPS/GLONASS/BDS except 18 March. The accuracy is

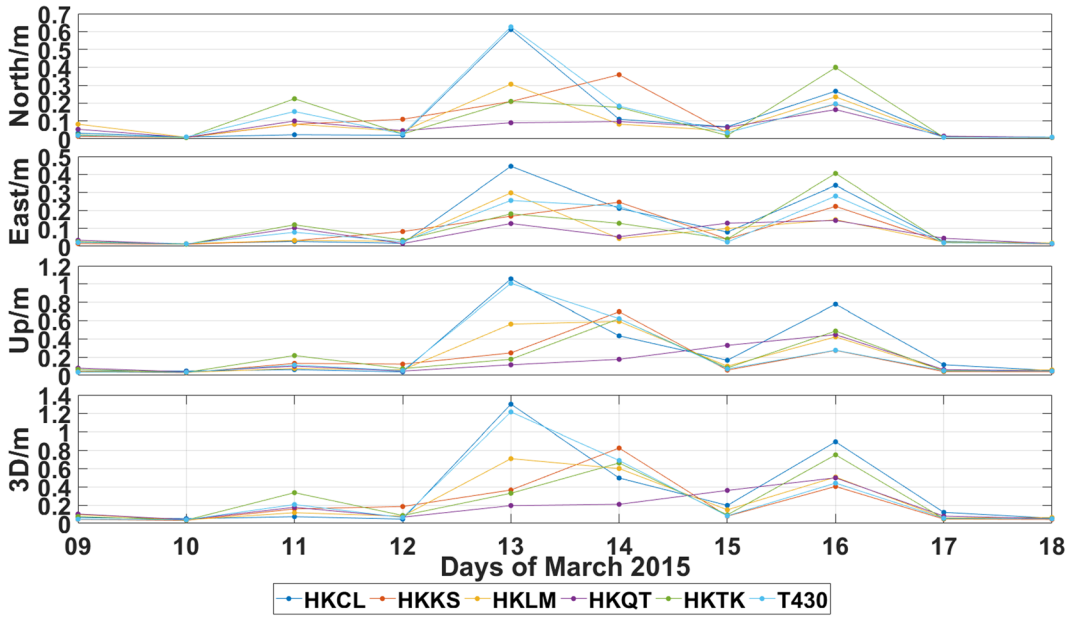

Figure 14. RMS of PPP with GPS only.

comparable for positioning results calculated with single-frequency observations and code IF observations on 18 March. Furthermore, it is also difficult to observe the direct relationship between positioning error and SNR fluctuations; it might be that the code MP noise is much higher than the noise generated by variation in SNR in this study.

The SPP results are rather stable during the ionospheric anomaly period both for GPS only and GPS/GLONASS/BDS. The fluctuation pattern of SPP solutions is inconsistent with that of ROTI, SNR, and MP from 9 to 16 March. On 17 March, there is absence of ionospheric anomaly, while the SPP accuracy is also lower than that of 18 March. After checking the global ionospheric condition, we found that Hong Kong is located in the ionospheric anomaly crest region from 9 to 17 March. Then we think the difference between Klobuchar model and real ionospheric conditions may contribute to the SPP accuracy decrease. The SPP results calculated with code IF combination observations also confirm this conclusion, though the direct correlation between SPP accuracy and SNR fluctuations is not observed.

4.3. PPP Performance With Multi-GNSS

In order to obtain high-precision positioning result with a single station, the Bernese5.2 and GAMP software are employed to process GPS only and GPS/GLONASS/BDS data, respectively, for kinematic PPP.

The PPP results of six stations at Hong Kong are shown in Figure 13. The obvious jump is observed on 9 to 16 March except 10 March, which is consistent with the fluctuations of ROTI. Different from other stations, a jump of solutions is also found on 10 March at HKCL. Furthermore, the kinematic PPP solutions of HKCL fluctuate a lot on 16 March, which results from frequent change of the visible satellite number due to some other reasons.

Figure 14 indicates the significant effect of space weather on PPP solutions on severe scintillation days. The strongest effect on PPP is on 13 March, on which the 3-D RMS is more than 1.3 m for HKCL and more than 1.2 m for T430. As shown in Figure 13, the growth of positioning error is mainly related to the periods of ionospheric anomalies.

In order to access the PPP performance with multi-GNSS under the effect of ionospheric anomalies, the open source software GAMP is employed to obtain PPP solutions with combined GPS/GLONASS/BDS, which are shown in Figure 15. As the different data processing strategies is adopted for GAMP and Bernese, the results obtained with GAMP (Figure 15) demonstrate a short convergence period at the beginning of every day. Except the convergence and reconvergence period, the systematic shift of positioning results with combined

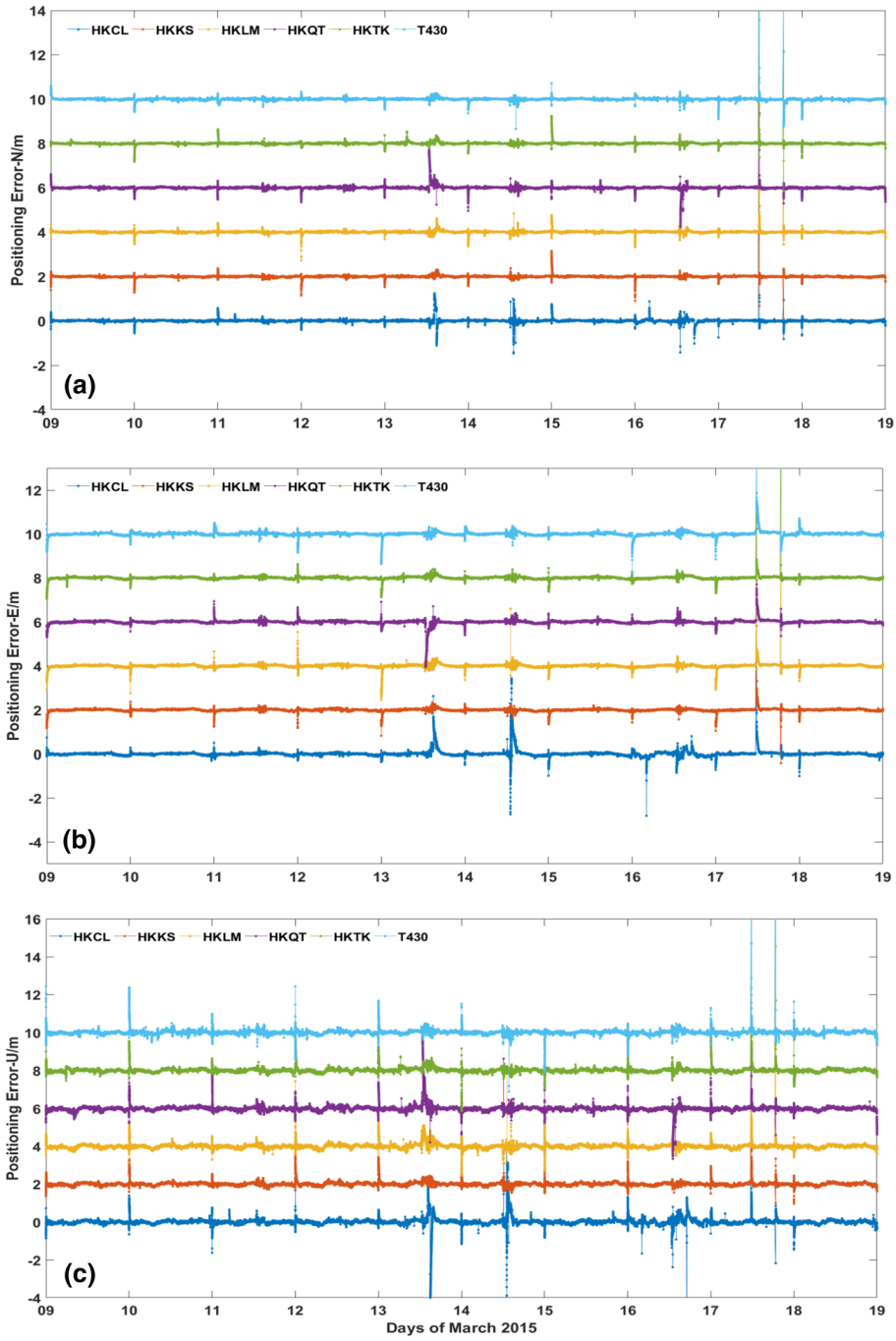

Figure 15. PPP results with GPS/GLONASS/BDS only at six stations in Hong Kong (the positioning error of each station was shifted by two additional meters except HKCL).

GPS/GLONASS/BDS is much smaller than that of GPS only (Figure 13). On 9 March, about 1 m jump is observed from the positioning error series, while there is no similar jump for combined solution.

For other days (12–16 March) and stations, obvious jump can be observed both for GPS only and GPS/GLONASS/BDS solutions during the scintillation period, while the positioning error of combined solution is much smaller than that of GPS only. On 13 March at T430, the positioning error of GPS only (Figure 13) is about 4, 2, and 6 m in north, east, and up directions, respectively. While for GPS/GLONASS/BDS solutions, they are only 0.25, 0.2, and 0.4 m in north, east, and up directions,

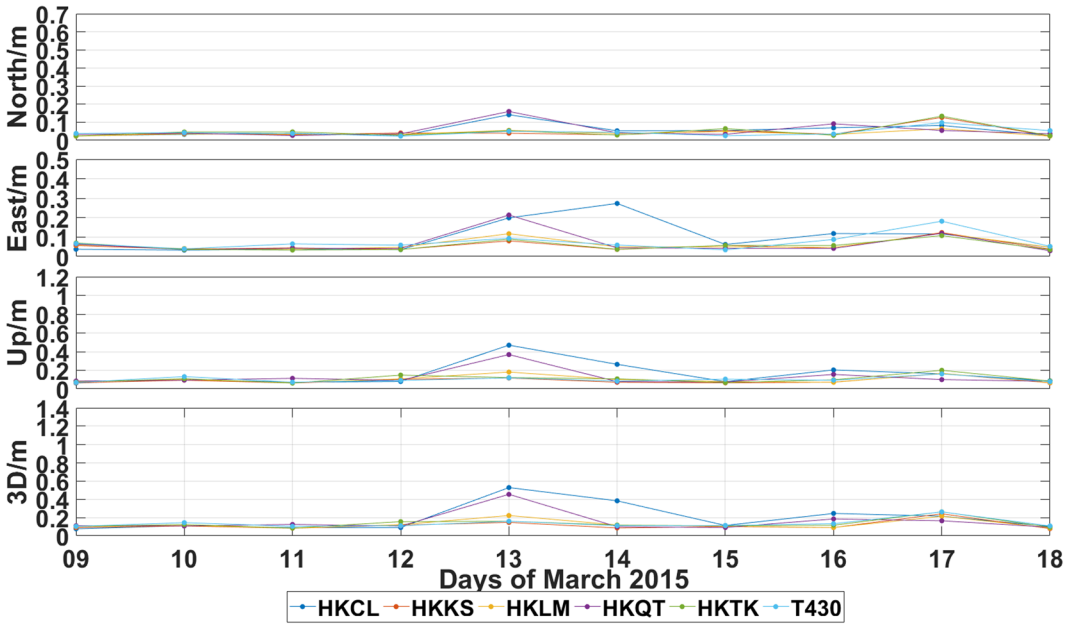

Figure 16. Statistical results of PPP with GPS/GLONASS/BDS.

respectively. The jumps of PPP solutions on 17 March for combined GPS/GLONASS/BDS result from the reconvergence for the LOL with unknown reason.

The RMS of combined solutions are shown in Figure 16, following the structure of Figure 14 (PPP with GPS only). The positioning accuracy is much higher than that of GPS only for the strong scintillation days. During 9, 10, 17, and 18 March, it seems that the accuracy of GPS only is relatively higher, which results from the different data processing strategies of GAMP and Bernese, and we include the solutions during the convergence period for combined solutions in the statistical results (Figure 16).

The fluctuations of PPP solutions are consistent with that of ROTI, SNR (except some unusual jump), and MP. The PPP positioning performance is strongly affected from 9 to 16 March, while the positioning accuracy return back to normal on 17 and 18 March, the main phase of the St. Patrick's geomagnetic storm. With the combination of GPS/GLONASS/BDS, the positioning accuracy is improved significantly during the strong ionospheric anomaly days. Figure 17 shows the PPP solutions with GPS only and the number

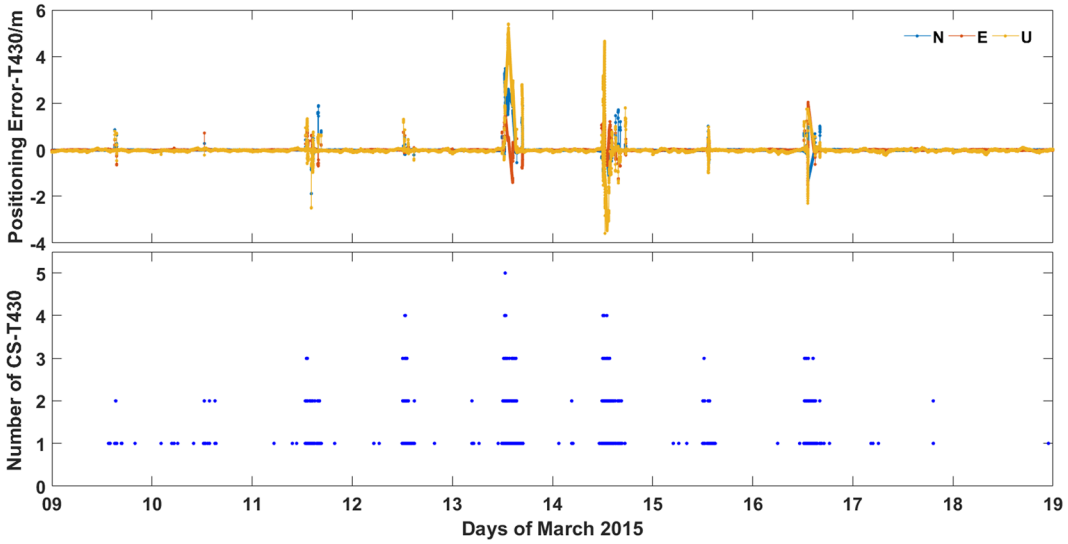

Figure 17. Comparison of GPS PPP solutions and GPS CS for T430.

of GPS CS for each epoch at T430. The direct relation between the PPP jumps and CS occurrence is observed. When the PPP solutions jump, the frequent CS occurred at corresponding time. The occurrence number and frequency of CS should be responsible for the duration and amplitude of PPP jumps. The more frequent the CS is observed, the PPP fluctuations may last longer and the amplitude would be larger. For example, comparing to other days, the CS occurrence is much more frequent on 13 and 14 March. Then the longer jumps of PPP solutions is observed at corresponding period; the amplitude is also much larger than other days. Thus, the solar flares may increase the ionospheric anomalies, which result in frequent CS. The jumps of PPP solutions mainly result from the subsequent reconvergence caused by frequent CS.

Overall, severe ionospheric scintillation would affect the GNSS positioning performance, especially for carrier phase-based positioning techniques due to frequent CS. Since the scintillation events will not affect all the visible satellites, the combination of multi-GNSS can improve the positioning performance significantly.

5. Discussions and Conclusions

In this contribution, the positioning performance with multi-GNSS is assessed around the St. Patrick's magnetic storm in 2015 in Hong Kong.

As reported, in the runup to the super magnetic storm, there are many solar X-ray flares, while the anomaly is absent for Kp, Dst, and AE indexes. After analyzing the ROTI series in Hong Kong, strong ionospheric scintillation events are observed from 9 to 16 March except 10 March, while there is no significant scintillation observed on 17 and 18 March. The X-ray solar flares might increase the ionospheric anomalies in this study as the TEC is more correlated with X-ray flux in equatorial and low-latitude region (Wang et al., 2006).

In order to analyze the effects of scintillation events on GNSS positioning service, the SNR and MP observables are employed to analyze the CS and LOL of GPS, GLONASS, and BDS carrier phase measurements. The SNR fluctuates a lot during the ionospheric anomaly period; the MP observable also demonstrates significant fluctuations at corresponding time due to the frequent CS and LOL and pseudorange error. The SNR and MP observables of L2 fluctuate more than that of L1, which indicates that the L2 is much more sensitive than L1.

Then the positioning performance of SPP and PPP with multi-GNSS is analyzed. The SPP is not advisable to observe effect of ionospheric scintillation due to inefficient Klobuchar ionospheric model. The fluctuations of PPP are consistent with corresponding ionospheric scintillation events both for GPS only and GPS/GLONASS/BDS. The PPP accuracy is decreased dramatically due to subsequent reconvergence led by frequent CS and LOL, which results from strong ionospheric anomalies. The maximum daily 3-D positioning error is about 1.3 m for GPS only, and the positioning error reaches several meters during strong scintillation period. As expected, the positioning performance is improved significantly with the combination of GPS, GLONASS, and BDS. The maximum daily 3-D positioning error is reduced to 0.6 m with multi-GNSS.

Future work will focus on ionospheric scintillation events detection with geodetic GNSS receiver and further improving positioning accuracy and availability with robust estimation both for PPP and RTK.

Conflicts of Interest

The authors declare no conflict of interest.

Acknowledgments

This study was supported by the Key Program of the National Natural Science Foundation of China (Grant 41631073), the Shandong Provincial Natural Science Foundation, China (Grant ZR2016DM15), the Open Fund of State Key Laboratory of Earthquake Dynamics (Grant LED2018B03), and Shenzhen Science and Technology Innovation Commission (Project JCYJ20170818104822282). Thanks to the Hong Kong Satellite Positioning Reference Station Network (SatRef) and IGS for providing the data used in this study. We would also like to thank the Editor and two anonymous reviewers for their valuable suggestions and comments. The Kp, Dst, and AE indexes for the storm were obtained from World Data Center (WDC, http://wdc.kugi.kyoto-u.ac.jp). The solar flare X-ray measurements are available on the National Oceanic and Atmospheric Administration (NOAA, https://www.ngdc.noaa.gov/stp/spaceweather.html). The GNSS RINEX data used in this paper are available on the Survey and Mapping Office (SMO) of Lands Department in Hong Kong (https://www.geodetic.gov.hk/en/satref/satref.htm). The open source software GAMP is available at www.ngs.noaa.gov/gps-toolbox/GAMP.

References

Amaechi, P. O., Oyeyemi, E. O., & Akala, A. O. (2018). The response of African equatorial/low-latitude ionosphere to 2015 St. Patrick's Day geomagnetic storm. *Space Weather*, *16*, 601–618. https://doi.org/10.1029/2017SW001751

Aquino, M., Monico, J. F. G., Dodson, A., Marques, H. A., Franceschi, G., Alfonsi, L., et al. (2009). Improving the GNSS positioning stochastic model in the presence of ionospheric scintillation. *Journal of Geodesy*, *83*(10), 953–966. https://doi.org/10.1007/s00190-009-0313-6

Astafyeva, E., Zakharenkova, I., & Förster, M. (2015). Ionospheric response to the 2015 St. Patrick's Day storm: A global multi-instrumental overview. *Journal of Geophysical Research: Space Physics*, *120*, 9023–9037. https://doi.org/10.1002/2015JA021629

Barbosa, F. R. E., Fagundes, P. R., Venkatesh, K., Fejer, B. G., Pillat, V. G., Denardini, C. M., & Muella, M. T. A. H. (2018). Multi-scale ionospheric irregularities occurrence over South America during the St. Patrick's Day storm on March 17, 2015. *Journal of Atmospheric and Solar-Terrestrial Physics*, *174*, 32–45. https://doi.org/10.1016/j.jastp.2018.05.001

Basu, S., MacKenzie, E., & Basu, S. (1988). Ionospheric constraints on VHF/UHF communications links during solar maximum and minimum periods. *Radio Science*, *23*(3), 363–378. https://doi.org/10.1029/RS023i003p00363

Berdermann, J., Kriegel, M., Banyś, D., Heymann, F., Hoque, M. M., Wilken, V., et al. (2018). Ionospheric response to the X9.3 flare on 6 September 2017 and its implication for navigation services over Europe. *Space Weather*, *16*, 1604–1615. https://doi.org/10.1029/2018SW001933

Bong, V. P., Abidin, W. A. W. Z., Abdullah, M., Ping, K. H., Masri, T., Bahari, S. A. & Abba, I. (2015). GPS signal strength due to ionospheric scintillation: Preliminary models over Sarawak. 2015 International Conference on Space Science and Communication (IconSpace).
Borries, C., Mahrous, A. M., Ellahouny, N. M., & Badeke, R. (2016). Multiple ionospheric perturbations during the Saint Patrick's Day storm 2015 in the European-African sector. *Journal of Geophysical Research: Space Physics*, *121*, 11,333–311,345. https://doi.org/10.1002/2016JA023178
Chen, C. H., Lin, C. H., Matsuo, T., & Chen, W. H. (2016). Ionosphere data assimilation modeling of 2015 St. Patrick's Day geomagnetic storm. *Journal of Geophysical Research: Space Physics*, *121*, 11,549–11,559. https://doi.org/10.1002/2016JA023346
Cherniak, I., Zakharenkova, I., & Redmon, R. J. (2015). Dynamics of the high-latitude ionospheric irregularities during the 17 March 2015 St. Patrick's Day storm: Ground-based GPS measurements. *Space Weather*, *13*, 585–597. https://doi.org/10.1002/2015SW001237
Conker, R. S., El-Arini, M. B., Hegarty, C. J., & Hsiao, T. (2003). Modeling the effects of ionospheric scintillation on GPS/satellite-based augmentation system availability. *Radio Science*, *38*(1), 1001. https://doi.org/10.1029/2000RS002604
da Silva, H. A., de Oliveira Camargo, P., Galera Monico, J. F., Aquino, M., Marques, H. A., De Franceschi, G., & Dodson, A. (2010). Stochastic modelling considering ionospheric scintillation effects on GNSS relative and point positioning. *Advances in Space Research*, *45*(9), 1113–1121. https://doi.org/10.1016/j.asr.2009.10.009
Dach, R., Andritsch, F., Arnold, D., Bertone, S., Fridez, P., Jäggi, A., et al. (2015). Bernese GNSS software Version 5.2.
Gao, S. (2008). Monitoring and modelling Hong Kong ionosphere using regional GPS networks, thesis (PhD)—the Hong Kong Polytechnic University, 2008.
He, Z., Zhao, H., & Feng, W. (2016). The ionospheric scintillation effects on the BeiDou signal receiver. *Sensors*, *16*(11), 1883. https://doi.org/10.3390/s16111883
Helmboldt, J. F., Kassim, N. E., & Teare, S. W. (2015). Observations of the ionospheric impact of M-class solar flares on local and hemispheric scales. *Earth and Space Science*, *2*, 387–402. https://doi.org/10.1002/2015EA000116
Hlubek, N., Berdermann, J., Wilken, V., Gewies, S., Jakowski, N., Wassaie, M. & Damtie, B. (2014). Scintillations of the GPS, GLONASS, and Galileo signals at equatorial latitude.
Jacobsen, K. S. (2014). The impact of different sampling rates and calculation time intervals on ROTI values. *Journal of Space Weather Space Climate*, *4*, A33. https://doi.org/10.1051/swsc/2014031
Jacobsen, K. S., & Andalsvik, Y. L. (2016). Overview of the 2015 St. Patrick's Day storm and its consequences for RTK and PPP positioning in Norway. *Journal of Space Weather Space Climate*, *6*, A9. https://doi.org/10.1051/swsc/2016004
Ji, S., Chen, W., Wang, Z., Xu, Y., Weng, D., Wan, J., et al. (2013). A study of occurrence characteristics of plasma bubbles over Hong Kong area. *Advances in Space Research*, *52*(11), 1949–1958. https://doi.org/10.1016/j.asr.2013.08.026
Ji, S., Chen, W., Weng, D., Wang, Z., & Ding, X. (2013). A study on cycle slip detection and correction in case of ionospheric scintillation. *Advances in Space Research*, *51*(5), 742–753. https://doi.org/10.1016/j.asr.2012.10.012
Jin, S., Jin, R., & Kutoglu, H. (2017). Positive and negative ionospheric responses to the March 2015 geomagnetic storm from BDS observations. *Journal of Geodesy*, *91*(6), 613–626. https://doi.org/10.1007/s00190-016-0988-4
Jin, Y., & Oksavik, K. (2018). GPS scintillations and losses of signal lock at high latitudes during the 2015 St. Patrick's Day storm. *Journal of Geophysical Research: Space Physics*, *123*, 7943–7957. https://doi.org/10.1029/2018JA025933
Kintner, P. M., Ledvina, B. M., & de Paula, E. R. (2007). GPS and ionospheric scintillations. *Space Weather*, *5*, S09003. https://doi.org/10.1029/2006SW000260
Klobuchar, J. A. (1987). Ionospheric time-delay algorithm for single-frequency GPS users. *IEEE Transactions on Aerospace and Electronic Systems*, *AES-23*(3), 325–331. https://doi.org/10.1109/TAES.1987.310829
Kuai, J., Liu, L., Liu, J., Sripathi, S., Zhao, B., Chen, Y., et al. (2016). Effects of disturbed electric fields in the low-latitude and equatorial ionosphere during the 2015 St. Patrick's Day storm. *Journal of Geophysical Research: Space Physics*, *121*, 9111–9126. https://doi.org/10.1002/2016JA022832
Liu, W., Jin, X., Wu, M., Hu, J., & Wu, Y. (2018). A new real-yime cycle slip detection and repair method under high ionospheric activity for a triple-frequency GPS/BDS receiver. *Sensors (Basel, Switzerland)*, *18*(2), 427.
Loewe, C. A., & Prölss, G. W. (1997). Classification and mean behavior of magnetic storms. *Journal of Geophysical Research*, *102*(A7), 14209–14213. https://doi.org/10.1029/96JA04020
Luo, X., Gu, S., Lou, Y., Xiong, C., Chen, B., & Jin, X. (2018). Assessing the performance of GPS precise point positioning under different geomagnetic storm conditions during solar cycle 24. *Sensors*, *18*(6), 1784. https://doi.org/10.3390/s18061784
Mahajan, K. K., Lodhi, N. K., & Upadhayaya, A. K. (2010). Observations of X-ray and EUV fluxes during X-class solar flares and response of upper ionosphere. *Journal of Geophysical Research*, *115*, A12330. https://doi.org/10.1029/2010JA015576
Marques, H. A., Marques, H. A. S., Aquino, M., Veettil, S. V., & Monico, J. F. G. (2018). Accuracy assessment of precise point positioning with multi-constellation GNSS data under ionospheric scintillation effects. *Journal of Space Weather Space Climate*, *8*, A15. https://doi.org/10.1051/swsc/2017043
Maurya, A. K., Venkatesham, K., Kumar, S., Singh, R., Tiwari, P., & Singh, A. K. (2018). Effects of St. Patrick's Day geomagnetic storm of March 2015 and of June 2015 on low-equatorial D region ionosphere. *Journal of Geophysical Research: Space Physics*, *123*, 6836–6850. https://doi.org/10.1029/2018JA025536
Nava, B., Rodríguez-Zuluaga, J., Alazo-Cuartas, K., Kashcheyev, A., Migoya-Orué, Y., Radicella, S. M., et al. (2016). Middle- and low-latitude ionosphere response to 2015 St. Patrick's Day geomagnetic storm. *Journal of Geophysical Research: Space Physics*, *121*, 3421–3438. https://doi.org/10.1002/2015JA022299
Nayak, C., Tsai, L. C., Su, S. Y., Galkin, I. A., Caton, R. G., & Groves, K. M. (2017). Suppression of ionospheric scintillation during St. Patrick's Day geomagnetic super storm as observed over the anomaly crest region station Pingtung, Taiwan: A case study. *Advances in Space Research*, *60*(2), 396–405. https://doi.org/10.1016/j.asr.2016.11.036
Ning, Y., & Tang, J. (2018). Study of ionospheric disturbances over the China mid- and low-latitude region with GPS observations. *Annales de Geophysique*, *36*(1), 81–89. https://doi.org/10.5194/angeo-36-81-2018
Pi, X., Mannucci, A. J., Lindqwister, U. J., & Ho, C. M. (1997). Monitoring of global ionospheric irregularities using the worldwide GPS network. *Geophysical Research Letters*, *24*(18), 2283–2286. https://doi.org/10.1029/97GL02273
Prikryl, P., Ghoddousi-Fard, R., Thomas, E. G., Ruohoniemi, J. M., Shepherd, S. G., Jayachandran, P. T., et al. (2015). GPS phase scintillation at high latitudes during geomagnetic storms of 7–17 March 2012—Part 1: The North American sector. *Annales de Geophysique*, *33*(6), 637–656. https://doi.org/10.5194/angeo-33-637-2015
Prikryl, P., Ghoddousi-Fard, R., Weygand, J. M., Viljanen, A., Connors, M., Danskin, D. W., et al. (2016). GPS phase scintillation at high latitudes during the geomagnetic storm of 17–18 March 2015. *Journal of Geophysical Research: Space Physics*, *121*, 10,448–410,465. https://doi.org/10.1002/2016JA023171

Priyadarshi, S. (2015). A review of ionospheric scintillation models. *Surveys in Geophysics*, *36*(2), 295–324. https://doi.org/10.1007/s10712-015-9319-1

Ray, J., Griffiths, J., Collilieux, X., & Rebischung, P. (2013). Subseasonal GNSS positioning errors. *Geophysical Research Letters*, *40*, 5854–5860. https://doi.org/10.1002/2013GL058160

Saastamoinen, J. (1972). Contributions to the theory of atmospheric refraction. *Bulletin Géodésique (1946–1975)*, *105*(1), 279–298. https://doi.org/10.1007/BF02521844

Shi, J., & Gao, Y. (2014). A comparison of three PPP integer ambiguity resolution methods. *GPS Solutions*, *18*(4), 519–528. https://doi.org/10.1007/s10291-013-0348-2

Shi, J., Yuan, X., Cai, Y., & Wang, G. (2017). GPS real-time precise point positioning for aerial triangulation. *GPS Solutions*, *21*(2), 405–414. https://doi.org/10.1007/s10291-016-0532-2

Sreeja, V. (2016). Impact and mitigation of space weather effects on GNSS receiver performance. *Geoscience Letters*, *3*(1), 24. https://doi.org/10.1186/s40562-016-0057-0

Sreeja, V., Aquino, M., Jong, K., & Visser, H. (2014). Effect of the 24 September 2011 solar radio burst on precise point positioning service. *Space Weather*, *12*, 143–147. https://doi.org/10.1002/2013SW001011

Steenburgh, R. A., Smithtro, C. G., & Groves, K. M. (2008). Ionospheric scintillation effects on single frequency GPS. *Space Weather*, *6*, S04D02. https://doi.org/10.1029/2007SW000340

Sun, W. J., Ning, B. Q., Zhao, B. Q., Li., G., Hu, L. & Chang, S. M. (2017). Analysis of ionospheric features in middle and low latitude region of China during the geomagnetic storm in March 2015.

Takasu, T. & Yasuda, A. (2009). Development of the low-cost RTK-GPS receiver with an open source program package RTKLIB.

Vadakke Veettil, S., Haralambous, H., & Aquino, M. (2017). Observations of quiet-time moderate midlatitude L-band scintillation in association with plasma bubbles. *GPS Solutions*, *21*(3), 1113–1124. https://doi.org/10.1007/s10291-016-0598-x

Vaishnav, R., Jacobi, C., Berdermann, J., Schmölter, E., & Codrescu, M. (2018). Ionospheric response to solar EUV variations: Preliminary results. *Advances in Radio Science*, *16*, 157–165. https://doi.org/10.5194/ars-16-157-2018

Vilà-Valls, J., Closas, P., & Curran, J. T. (2017). Multi-frequency GNSS robust carrier tracking for ionospheric scintillation mitigation. *Journal of Space Weather Space Climate*, *7*, A26. https://doi.org/10.1051/swsc/2017020

Wang, G., de Jong, K., Zhao, Q., Hu, Z., & Guo, J. (2015). Multipath analysis of code measurements for BeiDou geostationary satellites. *GPS Solutions*, *19*(1), 129–139. https://doi.org/10.1007/s10291-014-0374-8

Wang, X., Eastes, R., Weichecki Vergara, S., Bailey, S., Valladares, C., & Woods, T. (2006). On the short-term relationship between solar soft X-ray irradiances and equatorial total electron content (TEC). *Journal of Geophysical Research*, *111*, A10S15. https://doi.org/10.1029/2005JA011488

Xu, D., & Morton, Y. T. J. (2018). GPS navigation data bit decoding error during strong equatorial scintillation. *GPS Solutions*, *22*(4), 110. https://doi.org/10.1007/s10291-018-0775-1

Xu, R., Liu, Z., & Chen, W. (2015). Multi-PLL with two-stage fusion to mitigate ionospheric scintillation effects on GPS receivers. *Radio Science*, *50*, 630–641. https://doi.org/10.1002/2015RS005664

Yadav, S., Sunda, S., & Sridharan, R. (2016). The impact of the 17 March 2015 St. Patrick's Day storm on the evolutionary pattern of equatorial ionization anomaly over the Indian longitudes using high-resolution spatiotemporal TEC maps: New insights. *Space Weather*, *14*, 786–801. https://doi.org/10.1002/2016SW001408

Yang, Z., & Liu, Z. (2016). Observational study of ionospheric irregularities and GPS scintillations associated with the 2012 tropical cyclone Tembin passing Hong Kong. *Journal of Geophysical Research: Space Physics*, *121*, 4705–4717. https://doi.org/10.1002/2016JA022398

Yasyukevich, Y., Astafyeva, E., Padokhin, A., Ivanova, V., Syrovatskii, S., & Podlesnyi, A. (2018). The 6 September 2017 X-class solar flares and their impacts on the ionosphere, GNSS, and HF radio wave propagation. *Space Weather*, *16*, 1013–1027. https://doi.org/10.1029/2018SW001932

Zhang, X., Guo, F., & Zhou, P. (2014). Improved precise point positioning in the presence of ionospheric scintillation. *GPS Solutions*, *18*(1), 51–60. https://doi.org/10.1007/s10291-012-0309-1

Zhou, F., Dong, D., Li, W., Jiang, X., Wickert, J., & Schuh, H. (2018). GAMP: An open-source software of multi-GNSS precise point positioning using undifferenced and uncombined observations. *GPS Solutions*, *22*, 33. https://doi.org/10.1007/s10291-018-0699-9